ARTICLE　OPEN

Check for updates

Interlayer angle control of the electronic mini-gaps, band splitting, and hybridization in graphene–WS$_2$ moiré heterostructures

Francisco Hidalgo [1], Francisco Sánchez-Ochoa [1] and Cecilia Noguez [1] ✉

Understanding the electronic properties modulation in graphene/tungsten disulfide (G-WS$_2$) at different interlayer angles is essential for promising building blocks of two-dimensional (2D) heterostructures. G-WS$_2$ heterostructures with four different interlayer angles are studied using periodic first-principles calculations and an unfolding method to decipher the supercell crowded-band structure. Electronic mini-gaps of different sizes, band splittings, and band hybridizations are identified because of the interactions between out-of-plane orbitals from both layers. These electronic changes are modulated depending on the interlayer angle in a given energy window and space region. At the same time, the replicas emerging because of the superperiodic potential associated with moiré patterns also modify such electronic alterations, inducing new electronic repulsions or avoided crossings. Therefore, the number of mini-gaps as well as their energy values and positions are intrinsically related to the interlayer angle. Finally, it is anticipated that these results might be essential for designing the electronic properties of 2D heterostructures.

INTRODUCTION

Two-dimensional (2D) atomic layers that are vertically stacked by van der Waals (vdW) interactions to build heterostructures (2D–vdW–h) might have fascinating properties for potential applications in optoelectronics[1–15]. These hybrids could retain the pristine monolayers' main features while achieving unusual properties that cannot be obtained otherwise. As a consequence, the interest in identifying the electronic properties of these 2D–vdW–h has increased. Particularly in systems such as graphene (G) and transition metal dichalcogenides (TMDCs), where intensive research studies are conducted in systems like G/G, TMDC/TMDC, and G/TMDC[13–19]. Additionally, a new degree of freedom is present when two or more 2D layers are vertically stacked: the interlayer relative angle, θ, made between the crystallographic orientations of both monolayers. For instance, results in twisted G/ G exhibit critically dependent electronic and optical properties upon θ[13,20–23]. Nevertheless, how much impact the interlayer rotation has on the electronic spectrum still needs to be understood from a fundamental perspective.

Previous studies on G/TMDC have reported that G Dirac cones fall inside the band gap of the TMDC. In addition, they have found direct to indirect electronic transitions, the reduction of the TMDC band gap, and the opening of small gaps close to the Dirac cone, where this latter is now positioned at the Γ point in the reciprocal space[24–26]. Other works on G/TMDC also reported similar changes in the electronic band structure, where once again, the Dirac cone is at Γ after a rotation between monolayers[27–29]. Also, angle-resolved photoemission spectroscopic measurements (ARPES) show interlayer hybridization and mini-gaps with no significant charge transfer between monolayers[30,31]. Additionally, density functional theory (DFT) calculations have found significant changes in the deeper (higher) valence (conduction) regions assisted by an out-of-plane interaction by relatively weak vdW effects, such as the opening of π-band-energy gaps simultaneously with a splitting around the Γ point at -6.0 eV below the

Fermi level[32–34]. However, more detailed studies considering different interlayer relative angles are still awaiting.

This paper discusses the graphene/tungsten disulfide (G-WS$_2$) electronic properties studied with periodic density functional theory (DFT) calculations and analyzed using a general unfolding method that allows us the identification of the band alterations upon interlayer interactions at different angles. First, the physical cause of the G band structure mini-gaps and other electronic deviations is studied when $\theta = 0.0°$. Then, the relative twist-angle impact on the G electronic band structure is unveiled by analyzing G-WS$_2$ with relative $\theta = 10.9°$, $19.1°$, and $30.0°$. The electronic changes are mainly associated with avoided crossings and moiré replicas, which depend on the interlayer angle. A resume of the unfolding method is in the Supplementary Information, as well as the strain influence on the G-WS$_2$ electronic structure due to the commensurability imposed on the G and WS$_2$ layers with a given θ angle.

RESULTS AND DISCUSSION

Unfolding bands

The G-WS$_2$ heterostructures supercells with different relative angles, $\theta = 0.0°$, $10.9°$, $19.1°$, and $30.0°$, are constructed using the optimized lattice parameters of the individual unit cell layers, both with hexagonal symmetry but different lattice constants, $a_G = 2.44$ Å, and $a_{WS_2} = 3.16$ Å. The strain condition to obey the commensurability is applied on the graphene layer. The structural difference induces variations in the band structure and the electronic properties, such as a small p-doping in graphene but not a charge transfer. The commensurability condition imposes up to a strain of 3.6% of the G layer, which can be achieved experimentally[35]. The four fully-optimized G-WS$_2$ electronic band structures are found through periodic DFT calculations using the SIESTA code[36]. Then, we employ an unfolding method that allows us to analyze mutual interactions between layers more

[1]Instituto de Física, Universidad Nacional Autónoma de México, Ciudad de México, C.P. 04510, Mexico. ✉email: cecilia@fisica.unam.mx
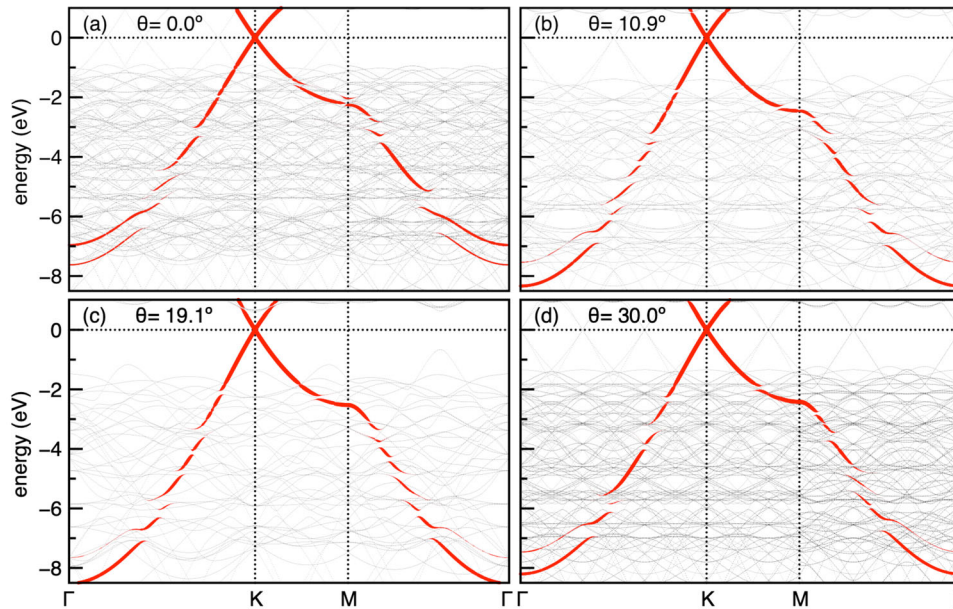
Fig. 1 Effective electronic bands projected onto graphene Brillouin zone for G-WS$_2$ at θ as the twist-angle. $\theta = $ **a** 0.0°, **b** 10.9°, **c** 19.1°, and **d** 30.0°. Red dots show projected SC electronic states onto graphene C(2p$_z$) electronic bands with $W_G > 0$, where dot sizes are proportional to W_G values. Tiny gray dots represent SC states with $W_G = 0$, i.e., states that do not originally belong to the isolated G layer in BZ$_G$. Here, E_F is set to 0 eV.

straightforwardly[37–43]. Details of the atomic models and computational calculations are described in the "Methods" section.

To analyze the results, first, we chose the irreducible Brillouin Zone (BZ) of pristine G or WS$_2$ primitive cells, delimited by the high-symmetry points over $\Gamma - K - M - \Gamma$ trajectories. Then, we obtain the effective electronic bands by projecting and comparing supercell (SC) electronic states to those of isolated G (WS$_2$) by employing the unfolding method. These are called in this work EEB$_G$ (EEB$_{WS_2}$). When comparing, we find that SC electronic states may belong completely ($W_{G/WS_2} = 1$), partly ($0 < W_{G/WS_2} < 1$), or nothing ($W_{G/WS_2} = 0$) to isolated G or WS$_2$, where a spectral weight, W_{G/WS_2}, is obtained for each electronic state. Thus, the spectral weight, W, measures how much of the electronic states of isolated monolayers are conserved in 2D–vdW–h upon the presence of other layers. This versatile unfolding method allows to project SC electronic states of G or WS$_2$ onto either primitive cell BZ, labeled BZ$_G$ or BZ$_{WS_2}$. Notice that the unfolding method employed here can project the electronic states distinguishing chemical species, atomic orbitals, and SC oriented at different angles concerning the original ones. For a detailed explanation, the reader can consult ref. [44].

Figure 1 shows the electronic band structure of the four G-WS$_2$ heterostructures along the irreducible BZ$_G$. The EEB$_G$ of projected out-of-plane Carbon 2p$_z$ orbitals or C(2p$_z$) electronic states are shown in red dots where dot size is proportional to W_G. Here, tiny gray dots represent SC electronic states with $W_G = 0$, i.e., those states that do not originally belong to the isolated G layer, such as electronic states resulting from the folded G layer or those belonging to WS$_2$. Comparing the four EEB$_G$ at different angles with the corresponding band of the isolated G monolayer, we immediately observe that two G properties are conserved. The Dirac point is in the Fermi level (E_F) and at the K point of the G primitive cell (PC$_G$), and EEB$_G$ shows a linear dispersion around the Dirac point. Contrarily, there are electronic differences from those known for isolated G, like multiple openings of the C(2p$_z$) bands and band splittings seen at Γ for energies smaller than -7 eV. These band openings are known as mini-gaps. For a quick reference, the band structure of isolated G is shown in the Supplementary Fig. 1(a). We do not include in Fig. 1 the bands

belonging to in-plane C orbitals, i.e., C(2s), C(2p$_x$), and C(2p$_y$), which are ~ -3 eV in Γ and disperse down to K and M, since they remain unaffected upon stacking on WS$_2$[44].

We remark that the affected G bands are composed solely of out-of-plane C(2p$_z$) orbitals, evidencing that electronic alterations come mainly from the mutual interaction with WS$_2$ electronic orbitals upon stacking. Looking at the four EEB$_G$, we find that band distortions and mini-gaps are localized at different points in the reciprocal space and occur at different energies, with θ as a parameter. For instance, the $\theta = 10.9°$ heterostructure shows the most significant number of mini-gaps and deviations of the C(2p$_z$) bands when going from $\Gamma \to K$ and between -6.0 and 0.0 eV. In contrast, the case with the smaller number of mini-gaps corresponds with $\theta = 30.0°$. To discuss these deviations, we first analyze the case with $\theta = 0.0°$, followed by the twisted-bilayer cases. The EEB$_G$ behaviors are examined in terms of (a) band foldings, (b) electronic repulsion between bands, and (c) the superperiodic potential influence. Band folding occurs because of the SC construction and gives rise to the so-called Bragg diffractions. Electronic repulsion between bands from different layers results in avoided crossings or mini-gaps. Finally, the superperiodic potential due to a second layer allows interactions with the so-called moiré replicas.

Bragg diffractions

Bragg diffractions occur when SC bands cross high-symmetry points or planes of either BZ$_G$ or BZ$_{WS_2}$, corresponding to the individual monolayers. Figure 2 shows BZs and Γ points represented with hexagons and dots, respectively. Here, green, blue, and red hexagons and dots correspond to the reciprocal space of the heterostructure, SC$_{G-WS_2}$, and the individual layers, PC$_{WS_2}$ and PC$_G$. Thus, green, red, and blue triangles show the corresponding irreducible BZs delimited by their high-symmetric points, Γ, K, and M. Notice that the Γ point (black label) at the concentric hexagons is the same for all, supercell and the primitive cells. Here, only K and M points of BZ$_G$ are identified with red labels. By following the $\Gamma \to K$ direction in BZ$_G$ (red triangle) when $\theta = 0.0°$, we identify four intersections with green vertices (V), all corresponding to the supercell K $-$ points. The third V intersection
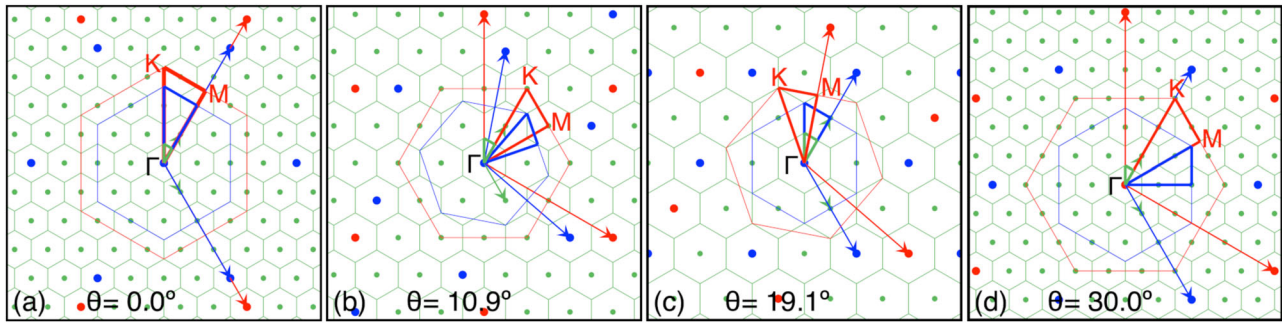
Fig. 2 Reciprocal spaces of G-WS$_2$ at θ as the twist-angle. $\theta =$ **a** 0.0°, **b** 10.9°, **c** 19.1°, and **d** 30°. Reciprocal spaces of G-WS$_2$ are shown in green hexagons. Red and blue hexagons depict G and WS$_2$ Brillouin zones, BZ$_G$ and BZ$_{WS_2}$, respectively. Γ points at BZ$_{G-WS_2}$, BZ$_G$, and BZ$_{WS_2}$ correspond to green, blue, and red dots. Reciprocal lattice vectors and irreducible BZs are shown with arrows and thick lines using the same color scheme. Γ, K, and M high-symmetry points of irreducible BZ$_G$ are labeled.

Table 1. Intersections between the irreducible BZ$_G$ with either BZs$_{SC}$ and BZ$_{WS_2}$ along the $\Gamma \rightarrow K \rightarrow M$ path[a].

Intersection (BZ)	$\theta = 0.0°$	10.9°	19.1°	30.0°
$\Gamma \rightarrow K$				
B (SC)	0	2	1	3
V (SC)	4	0	1	0
R (SC)	1	2	0	3
P (SC)	2	0	0	0
B (WS$_2$)	0	1	1	1
V (WS$_2$)	1	0	0	0
P (WS$_2$)	1	0	0	0
K$\rightarrow$M				
B (SC)	0	1	1	2
V (SC)	1	0	0	0
R (SC)	1	1	0	1
P (SC)	1	0	0	0
B (WS$_2$)	0	0	0	0
V (WS$_2$)	0	0	0	0
M$\rightarrow\Gamma$				
B (SC)	3	0	1	0
V (SC)	0	2	0	3
R (SC)	2	0	0	1
P (SC)	0	1	0	2
B (WS$_2$)	0	1	1	0
V (WS$_2$)	1	0	0	1
P (WS$_2$)	1	0	0	1
Total	19	11	6	18

[a]They are associated with borders (B), vertices (V), reciprocal-lattice points (R), and alongside part of the perimeter (P), belonging to either SC or WS$_2$ Brillouin zones.

also coincides with the K point of the WS$_2$ monolayer. Also, two segments of $\Gamma-K$ coincide with the borders or perimeters (P) of BZ$_{SC}$, and the fifth intersection is with one Γ_{SC} point or reciprocal lattice point (R). Notice that cone replicas at vertices and supercell K$-$points are visible in Fig. 1a by looking at the tiny gray dots close to E$_F$. The same happens with the other G-WS$_2$ hetero-structures with $\theta \neq 0°$. A list of the different V, P, and R intersections of the four G-WS$_2$ systems is in Table 1.

In Fig. 3a, the G irreducible BZ is shown where the intersections with supercell and WS$_2$ BZs are marked with dashed lines and labeled from 1 to 10, besides Γ, K, and M points of G. On the left-right side, the ten vertical dashed lines are at $k-$ points of such intersections, also labeled from 1 to 10, where the EEB$_G$ of C(2p$_z$) orbitals when $\theta = 0.0°$ is displayed. Notice that states with $W_G = 0$ are no longer shown. Here, we indicate some of the most representative alterations of EEB$_G$, where orange and black arrows correspond to Bragg diffractions and avoided crossings (C$_n$), respectively. At the same time, the distortions indicated by pink arrows (R$_n$) cannot be associated with any of these electronic features but with moiré replicas that we will discuss later. Recall that these characteristics are always present in the G-WS$_2$ SC band structure; however, they cannot be elucidated before the unfolding process, which also assigns spectral weights and exposes the electronic changes after stacking.

In Fig. 3(b), the vertical dashed lines from 1 to 4 in the $\Gamma-K$ path indicate where Bragg diffractions can be found. Notice that the first intersection takes place at Γ being the same for all BZs, i.e., G, WS$_2$, and G-WS$_2$, while the last one happens at K, where also is located the K$-$point of the SC. Hence, band gaps due to Bragg diffractions are expected to appear on those intersections, as such as those of WS$_2$. Like the one occurring at vertical line 1, located close to -6.5 eV and pointed out with an orange arrow, where an imperceptible distortion of the C(2p$_z$) band takes place. In the middle between the 4th line and K, there is the M$_{SC}$ high-symmetry point of the supercell, which induces a tiny alteration of the band, also observed in EEB$_G$ and pointed by an orange arrow. In general, we find that Bragg diffractions induce minimal band alterations. For instance, a more significant band opening is observed at the intersection with line 4, corresponding to a vertex in the SC. However, at this point, also a band repulsion is observed because of the moiré superpotential, as we will discuss later.

Doing the same analysis for K$\rightarrow$M, first, we find an intersection with a green dot (line 5), followed by a green vertex (line 6), and then continue alongside part of the green perimeter reaching an M point of the SC at the same place of the M point of graphene. Again, a minimal band alteration of the C(2p$_z$) band is found in line 5. At the vertex or line 6, a more considerable distortion of C(2p$_z$) is appreciated showing a gap; however, this gap results from a cone replica because of the moiré superpotential, as we discuss in the last part of this section. Finally, the M $\rightarrow \Gamma$ trajectory has two intersections with green borders (B) and two with green dots (R), shown with four vertical lines labeled as 7, 8, 9, and 10. Bragg diffractions are not visible along this segment, and the large band deviations suggest another kind of interaction. Because of the absence of vertices along this path (see Fig. 2), there are no cone replicas on this segment of Fig. 1a. Therefore, the origin of such band mini-gaps comes from electronic repulsions, as discussed in the following subsection.

Finally, the analysis of the DOS partial contributions in Fig. 4b–e supports the above observations. Band deviations marked with orange arrows are indistinguishable in DOS compared to the
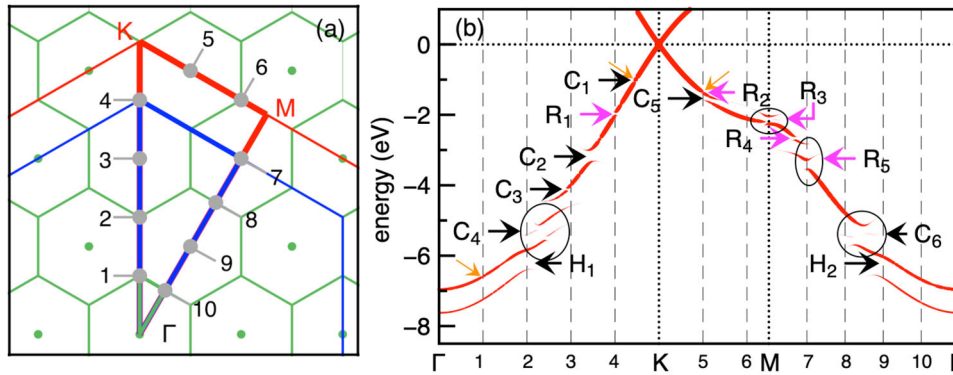
Fig. 3 Irreducible Brillouin zone and effective electronic bands of G-WS$_2$. a $k-$ points intersections between the G irreducible BZ with supercell and WS$_2$ BZs marked with gray dots and labeled from 1 to 10, besides intersections at Γ, K, and M points. **b** EEB$_G$ of C(2p$_z$) bands for G-WS$_2$ 2D–vdW–h with $\theta = 0°$ and $W_G > 0$, where dot size is proportional to W_G. Orange, black, and pink arrows indicate mini-gaps corresponding to Bragg diffractions, avoided crossings labeled as C$_n$, and moiré replicas labeled as R$_n$. The ten vertical dashed lines represent the $k-$ points where the intersections occur, marked on **a** in gray dots.
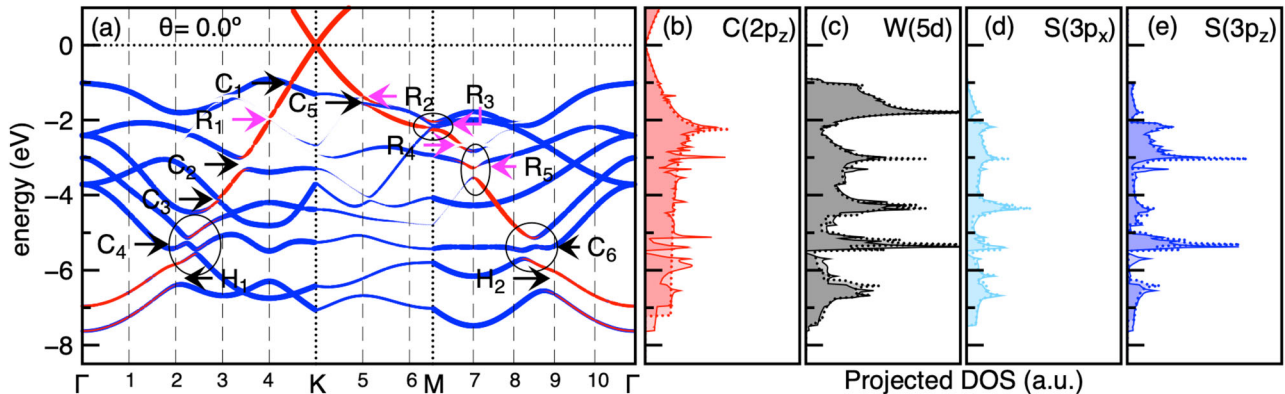

Fig. 4 Effective electronic bands of G-WS$_2$ and projected density of states. a EEB of G-WS$_2$ with $\theta = 0.0°$ projected onto BZ$_G$. Red and blue dots represent C(2p$_z$) and WS$_2$ bands. Dot size is proportional to the weights W_{G/WS_2}. **b–e** Show in solid lines the partial DOS corresponding to C(2p$_z$), W(5d), S(3p$_x$), and S(3p$_z$) orbitals. Also, the DOS of isolated monolayers in dotted lines are shown for comparison.

components of isolated G and WS$_2$. For the Bragg diffractions close to E_F, slight deviations of DOS are observed but only if such diffractions occur at the same place with other kinds of interactions like moiré replicas, as mentioned before. To corroborate the existence of Bragg diffractions, we construct the same G-WS$_2$ heterostructure with $\theta = 0.0°$ but placing an interlayer distance larger than the equilibrium one, for instance, at 5.5 Å. At this layer separation, we assure that mutual interactions between layers significantly decrease. After unfolding, EEB$_G$ is identical to pristine G, where all mini-gaps and band alterations in Fig. 3b have disappeared. The reader can see the Supplementary_movie_1.mp4 file in the Supplementary Information, an animation of the mutual interlayer interaction as a function of the interlayer separation.

Avoided crossings

The electronic repulsion between bands breaks them resulting in mini-gaps, also known as avoided crossings gaps, which may take place at any point of the BZ. To visualize them, we project all WS$_2$ (blue dots) and G C(2p$_z$) bands (red dots) on the irreducible BZ$_G$, as shown in Fig. 4a for G-WS$_2$ with $\theta = 0.0°$. The WS$_2$ projected states are beyond its irreducible BZ$_{WS_2}$, as seen in Fig. 2a. For instance, the K$_{WS_2}$ symmetry point of WS$_2$ is at line 4, while M$_{WS_2}$ coincides with line 7. Recall that the highest occupied band is in the WS$_2$ monolayer at K$_{WS_2}$, reproduced in Fig. 4a at line 4. Here, some mini-gaps are related to the mutual band crossing between

G and WS$_2$ bands. We use the same black arrows and C$_n$ as before to label avoided crossings. Because not all WS$_2$ bands interact with those of G, not all the overlappings between G and WS$_2$ bands generate gaps, but only those interacting with C(2p$_z$) and some WS$_2$ orbitals. By projecting the EEB$_{WS_2}$ for each orbital of WS$_2$ and looking at those that changed, we gain insights into interlayer interactions. In particular, we find that WS$_2$ bands with S(3p$_z$) orbitals interact with G, while bands without these orbitals do not. For example, the WS$_2$ band at about -4.2 eV between lines 7 and 8 is constituted by W(5d$_{xz}$), W(5d$_{yz}$), S(3p$_x$), and S(3p$_y$) orbitals, which overlaps C(2p$_z$) band but do not interact.

Mini-gaps marked with black arrows and labeled as C$_n$ in Figs. 3a and 4 come from out-of-plane orbitals interactions. For instance, the avoided crossing C$_2$ located between lines 3 and 4 at ~ -3.2 eV is mainly constituted by S(3p$_z$) orbitals, although W(5d$_{xz}$), W(5d$_{yz}$), S(3p$_x$), and S(3p$_y$) are also present but with a smaller spectral weight. The electronic repulsion in C$_2$ opens a gap of ~ 0.3 eV in both bands belonging to G and WS$_2$, where a kind of resonance is found that shows a mixing between G and WS$_2$ orbitals at the top and bottom of the mini-gap, giving continuity of the upper and bottom bands. These bands suggest that at such $k-$ point and energy, an electron on the G layer will move to WS$_2$ one and vice-versa. In addition, Fig. 4b–e panels show the C(2p$_z$), W(5d), S(3p$_x$), and S(3p$_z$) contributions to the total electronic density of states (DOS) of G-WS$_2$, respectively, as solid lines. For comparison, we also include the partial DOS corresponding to

both isolated layers in dotted lines. We do not include the partial DOS of in-plane C orbitals because they remain unperturbed upon the presence of WS_2, as we mentioned above.

The depletion in the $C(2p_z)$ and $S(3p_z)$ DOS components ~−3.2 eV, shown in Fig. 4b, e, confirm the presence of the mini-gap, delimited by two sharp peaks at about −3.0 and −3.3 eV. Similar behavior occurs for C_6 between lines 8 and 9, at ~−5.5 eV, where the $C(2p_z)$ band crosses two different WS_2 bands, exhibiting two well-defined gaps. Here, both WS_2 bands are constituted mainly by $S(3p_z)$ orbitals, but there is also the presence of $W(5d_{yz})$, $W(5d_{z^2})$, $W(5d_{xz})$, $S(3p_x)$, and $S(3p_y)$ orbitals. Again, partial DOS confirms this gap by two depletions of $C(2p_z)$ states centered at −5.2 and −5.5 eV. In contrast, C_1 exhibits a tiny gap between lines 4 and K at ~−1.0 eV. Despite this, the WS_2 band is mainly by in-plane $W(5d_{xy})$ and $W(5d_{x^2-y^2})$ orbitals, while $S(3p_z)$ shows a minor contribution according to their spectral weights. Nevertheless, this small amount of $S(3p_z)$ orbitals induces a tiny perturbation on the $C(2p_z)$ band. Another interesting case occurs in line 7 ~−3.0 eV pointed by a pink arrow. Again, we find a small contribution from $S(3p_z)$ orbitals; however, the band distortion is quite significant. In this case, the branch of the $S(3p_z)$ band is pushed up to higher energies by ~0.4 eV, simultaneously that the $C(2p_z)$ branch is spelled down, evidencing that another electronic interaction concurs additionally to the direct electronic repulsion. It is why we denoted these kinds of mini-gaps, like R_n rather than a C_n. We will discuss this new type of interaction below when we expose the role of interlayer rotations on electronic properties.

At M, about −2.2 eV, many bands converge that are mainly constituted by $S(3p_y)$ and $W(5d_{z^2})$ orbitals, labeled as R_3 in Fig. 4a. At the same time, $S(3p_x)$, $W(5d_{xy})$, and $S(3p_z)$ are also present with a smaller W. Although all these bands cross in a highly symmetric point, a significant band deviation results from the presence of $S(3p_z)$ orbitals. The slights deviations on DOS of $C(2p_z)$ and $S(3p_z)$ orbitals (see Fig. 4b, e) confirm the slight band distortion, such that the peak at −2.2 eV of $C(2p_z)$ decreases. Moreover, the large deviation and the small W of the $S(3p_z)$ orbitals indicate another kind of interaction. Again, we will go back to this type of band alteration when discussing the role of the interlayer angle in EEB. Between lines 2 and 3, from ~−4.0 to ~−5.5 eV, we find C_3 and C_4, where the $C(2p_z)$ band breaks in multiple small branches because of avoided crossings with the $S(3p_z)$ band and the bands made of $S(3p_x)$, $S(3p_y)$, and $S(3s)$ orbitals, which are all degenerated. These branches show an extended mixing of $C(2p_z)$ and WS_2 orbitals, resembling a hybridization. The two sharp peaks in DOS at ~−5.4 and −5.7 eV confirm this, Fig. 4b–e. Moreover, the short branch inside lines 2 and 3, at ~−5.0 eV, bands emerge from a band splitting and the band hybridization, which is inexistent in the isolated WS_2 and G layers, as seen in Supplementary Fig. 1a, b. Such band splitting disappears as we increase the distance among

layers (see the Supplementary_movie_1.mp4 file in the Supplementary Information).

The two bands at lower energies at Γ dispersing up (down) to line 2 (line 8), marked by H_1 (H_2) in Fig. 4a, reveal their hybridization nature between $C(2p_z)$ and WS_2 orbitals. In line 2, both $C(2p_z)$ and WS_2 bands split into two hybridized bands at ~−5.9 and ~−6.6 eV, dispersing down to reach Γ at ~−6.9 and ~−7.6 eV, respectively. A similar situation is observed inside lines 8 and Γ at around the same energies. From isolated G and WS_2 band structures, we observe only one band around this region instead of two. Thus, these hybridized bands emerge as a consequence of mutual interaction. Both hybridized bands have different spectral weights. For instance, the upper band exhibits more G character than WS_2, while the bottom one shows a more significant WS_2 nature. Confirming this hybridization, DOS shows a decrease of $C(2p_z)$ states of about half of its value compared to pristine G at −6.9 eV and extending up to −7.6 eV. Also, the amount of $S(3p_z)$ DOS diminishes and extends up to −7.6 eV, where the isolated WS_2 layer does not exhibit any occupied states. These hybridized states are mainly constituted by out-of-plane orbitals, while $S(3p_{x,y})$ and W orbitals remain unperturbed for energies below −6.5 eV. Graphite shows the same band splitting at about this energy[45], due to the vertical stacking of G layers. Here, WS_2 breaks the band degeneracy similarly to that of multiple G layers in graphite.

The remaining mini-gaps indicated with black arrows arise from avoided crossings between $C(2p_z)$ and $S(3p_z)$ orbitals. However, mini-gaps marked with pink arrows and labeled as R_n neither come strictly from avoided crossings or Bragg diffractions. For example, $S(3p_z)$ orbitals are absent around line 4 at ~−2.0 eV and line 7 at ~−2.7 eV, where R_1 and R_4 indicate small mini-gaps, respectively. The origin of these mini-gaps is attributed to the superperiodic potential due to the moiré pattern. Finally, we observe in Figs. 2a and 3a that lines 4 and 7 coincide with the K and M high-symmetry points of the irreducible BZ of the isolated WS_2, suggesting a repulsive interaction with moiré replicas. In the next section, we discuss the origin of R_n mini-gaps.

Moiré replicas

Moiré replicas emerge in 2D–vdW homo and heterostructures because of the superperiodic potential induced by the lattice mismatch between layers, visualized as moiré patterns[46]. In G-WS_2 with $\theta = 0.0°$, the reciprocal lattice vectors, $\mathbf{G}_G$ and $\mathbf{G}_{WS_2}$, shown in Fig. 2a, are different since G, and WS_2 lattice parameters also do. Moiré reciprocal lattice vectors defined as $\mathbf{G}_M = \mathbf{G}_G - \mathbf{G}_{WS_2}$ describe a superperiodic potential. In particular, the superpotential gives rise to six satellite cone replicas around each K point in BZ_G[46]. We show these satellite locations with black circles in Fig. 5a, which delimit a mini BZ also drawn in black lines. In general, any linear combination of $\mathbf{G}_G$ and $\mathbf{G}_{WS_2}$ represents a scatterer point that might show a complex pattern[47]. For instance,
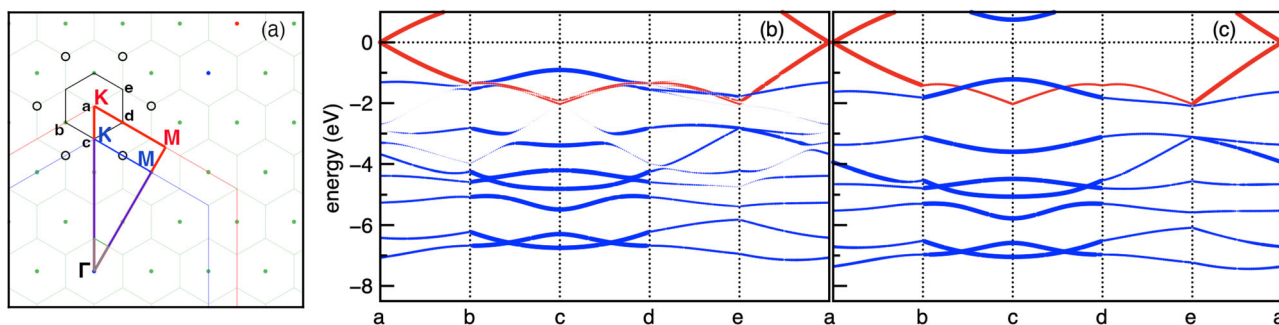

Fig. 5 Effective electronic bands around mini Brillouin zone. a Cone replicas around the K point bordering half of the mini BZ shown in black circles. **b** EEB_G and EEB_{WS_2} along the $a-b-c-d-e-a$ path at the equilibrium interlayer distance (with interactions), and **c** at 5.5 Å, where interlayer interactions are negligible.

Pletikosić and collaborators[46] reported mini-gaps for G supported on Ir(111) due to moiré replicas localized at the Bragg planes borders delimiting the mini BZ[46].

In our case, we found that the $\Gamma-K$ trajectory intersects the mini BZ at the reciprocal point, corresponding to line 4 in Fig. 3a or point c in Fig. 5a. Also, the $K-M$ path intersects the mini BZ, now corresponding to line 5 or point d, where a small gap is found at an energy of ~ -1.2 eV, as discussed above. To look deeper at these moiré replicas, we examine both EEB_G and EEB_{WS_2} with and without interactions between the two layers. These are shown in Fig. 5b, c, where EEB_G and EEB_{WS_2} are displayed along the path delimited by the cone replicas, i.e., $a \to b \to c \to d \to e \to a$. In this reciprocal region, the electronic bands predominantly belong to WS_2 (blue dots) and only one to $C(2p_z)$ (red dots). The main band distortions in G and WS_2 upon interlayer interactions (Fig. 5b) appear in the $b-c-d$ region at energies between -1.0 and -4.0 eV. One should notice that these distortions are present even in the absence of avoided crossings between G and WS_2 bands, revealing the superperiodic potential effects associated with the moiré pattern. By isolating both layers, i.e., separating them at a distance larger than the equilibrium one, the mutual interactions drop out. This later is shown in Fig. 5c, where both EEBs demonstrate that all the band distortions disappear when the layers are at 5.5 Å.

From this analysis, we found that all mini-gaps labeled as R_n and marked with pink arrows in Fig. 3(a) and Fig. 4 are related to the superperiodic potential or replicas and not to the direct EEB_G and EEB_{WS_2} bands crossings. Indeed, these mini-gaps appear from the electronic repulsions between bands belonging to G primitive cell and moiré replicas of both G and WS_2 unit cell. Because of the size of the G-WS_2 supercell with $\theta = 0.0°$, we cannot analyze in detail all R_n whether each mini-gap is associated with G or WS_2 replicas. However, a specific examination can be done for the smallest supercell that helps to elucidate the main features, as discussed in the next subsection.

So far, we have found that avoided crossings and moiré replicas are essential to explain the changes in the electronic bands in 2D-vdW heterostructures. These phenomena are related to the reciprocal spaces of SC and each isolated layer. In comparison, Bragg diffractions are responsible for the smaller electronic alterations, which are pretty much insignificant. On the other hand, avoided crossings open well-defined mini-gaps mainly because of the interactions between $C(2p_z)$ and $S(3p_z)$ out-of-plane orbitals. At deeper energies, these are hybridized, breaking the degeneration of both $C(2p_z)$ and $S(3p_z)$ bands. Then, moiré replicas arise from the superperiodic potential associated with the lattice mismatch between layers, which are characterized by mini BZs that also produce well-defined mini-gaps. Thus, all these electronic changes strongly depend on the supercell's symmetry. Therefore, it is expected that the relative angle between the top and bottom layers would play a fundamental role in controlling the electronic properties of moiré G-WS_2 heterostructures.

Mini-gaps assisted by the interlayer relative angle

To understand how the interlayer relative angle, θ, influences the electronic properties of G-WS_2 2D-vdW heterostructures, let us first discuss the case with $\theta = 30.0°$ by doing a similar analysis as done above. From Fig. 2d and following the $\Gamma-K$ path in BZ_G (red triangle), we found four crosses with vertices, where the latter is the K point of BZ_G. Hence, between the Γ and K points, there are 3 cone replicas. We also found that the $\Gamma-K$ trajectory crosses two green borders, while along $K-M$ there is one reciprocal-lattice point and two green borders, and along $M-\Gamma$ there are three green vertexes, one reciprocal-lattice point, and one green border. In this case, the BZs of G and WS_2 do not coincide except part of their borders, $M_G-\Gamma$ (red line) and $\Gamma-K_{WS_2}$ (blue line). On the other hand, both K-M paths for $\theta = 0.0°$ and 30.0° cases are outside the

first BZ_{WS_2} and do not intersect any of its high-symmetry points. This latter is true for the other two angles, $\theta = 10.9°$ and 19.1°, studied here. Notice that although the irreducible BZ_G is the same for both $\theta = 0.0°$ and 30.0° heterostructures, the intersections with the supercell's high-symmetry points are different (see Table 1). Additionally, we observe that $\theta = 0.0°$ and 30.0° exhibit the largest number of intersections with vertexes, reciprocal-lattice points, and borders. In contrast, the $\theta = 19.1°$ case has the smallest intersections followed by the $\theta = 10.9°$ heterostructure. The above discussion about the similarities and differences in the BZ paths for each θ, together with a comparison of bands' dispersions with and without interactions, will make it straightforward to determine the mini-gaps nature.

To expose the bands causing avoided crossings and their reliance on the twisted angle, in Fig. 6 we show $C(2p_z)$ and $S(3p_z)$ bands in red and blue dots, respectively, both projected into the irreducible BZ of G for the four angles studied here. Left-hand side panels, a–d, correspond to isolated or non-interacting G and WS_2 monolayers, while right-hand side panels, a'–d', show the same bands but for the interacting G-WS_2 heterostructures. The highest occupied band belonging to WS_2 is composed with the combination of $S(3p_z)$ and $W(5d_{z^2})$ orbitals with the same symmetry, where contributions from $W(5d_{z^2})$ orbitals are mainly observed in the highest-occupied band. In both left-handed and right-handed panels in Fig. 6, the labels C_n, H_n, and R_n are displayed to locate the mini-gaps upon interaction.

The band analysis shows that close to -7.0 eV at about the middle of $\Gamma-K$ and $M-\Gamma$ trajectories, the band hybridization open gaps, labeled as H_1 and H_2, observed for all twisted angles θ. These band splittings in Fig. 6a'–d' originate from the crossing and overlapping of $C(2p_z)$ and $S(3p_z) + W(5d_{z^2})$ bands, as noticed in the corresponding left-hand side panels. The energies at which H_1 and H_2 occur are slightly different for each θ. However, we should consider that the commensurability condition to treat G-WS_2 2D-vdW heterostructures like periodic systems might induce some tensile or compressive strengths on G, slightly altering those energies. As discussed in the Supplementary Methods: graphene under strain, mechanical effect modifies the $C(2p_z)$ band dispersion and induces small energy changes on WS_2 bands with respect to E_F. The tiny energy shift on WS_2 bands might be associated with an electrostatic screening that changes as the C to S atoms ratio does. This latter is also influenced by the G strain itself. For more details about the commensurability and its consequences on G-WS_2 bands, see the Supplementary Methods: graphene under strain.

Among the four cases, when $\theta = 0.0°$ the tensile condition is maximum and the $C(2p_z)$ and $S(3p_z)$ bands are practically superposed from Γ at ~7.0 eV to halfway K and M, as seen in Fig. 6(a). Here, the energy difference between such bands at Γ before interacting is only $\delta = 0.173$ eV. In contrast, when $\theta = 30.0°$ the heterostructure has the smallest compression, and the bands energy difference is about $\delta = 0.258$ eV (see Fig. 6d). Additionally, when $\theta = 10.9°$ bands separation is $\delta = 0.357$ eV (see Fig. 6b), while the case with maximum compression is $\theta = 19.1°$ also with the largest energy difference, $\delta = 0.487$ eV (see Fig. 6c). Note that G has a tensile condition when $\theta = 0.0°$, while it is compressed for $\theta = 10.9, 19.1,$ and 30.0°, exchanging the bands' energy order at Γ. In the first case a red band is followed by a blue one at deeper energy, while for the other angles, the blue band is followed by a red one.

Comparing the same regions in G-WS_2 before and upon interaction in Fig. 6, it is found that the H_1 and H_2 gaps are originated at the intersection between $S(3p_z)$ and $C(2p_z)$ bands. Moreover, $\theta = 0.0°$ shows a band repulsion with an energy gap of $\Delta E = 0.665$ eV, where $S(3p_z)$ and $C(2p_z)$ orbitals are combined and split into two bands, where the one pushed down shows more a $S(3p_z)$ component, while the one pushed up has more $C(2p_z)$ character. In contrast, when $\theta = 10.9, 19.1,$ and 30.0° the
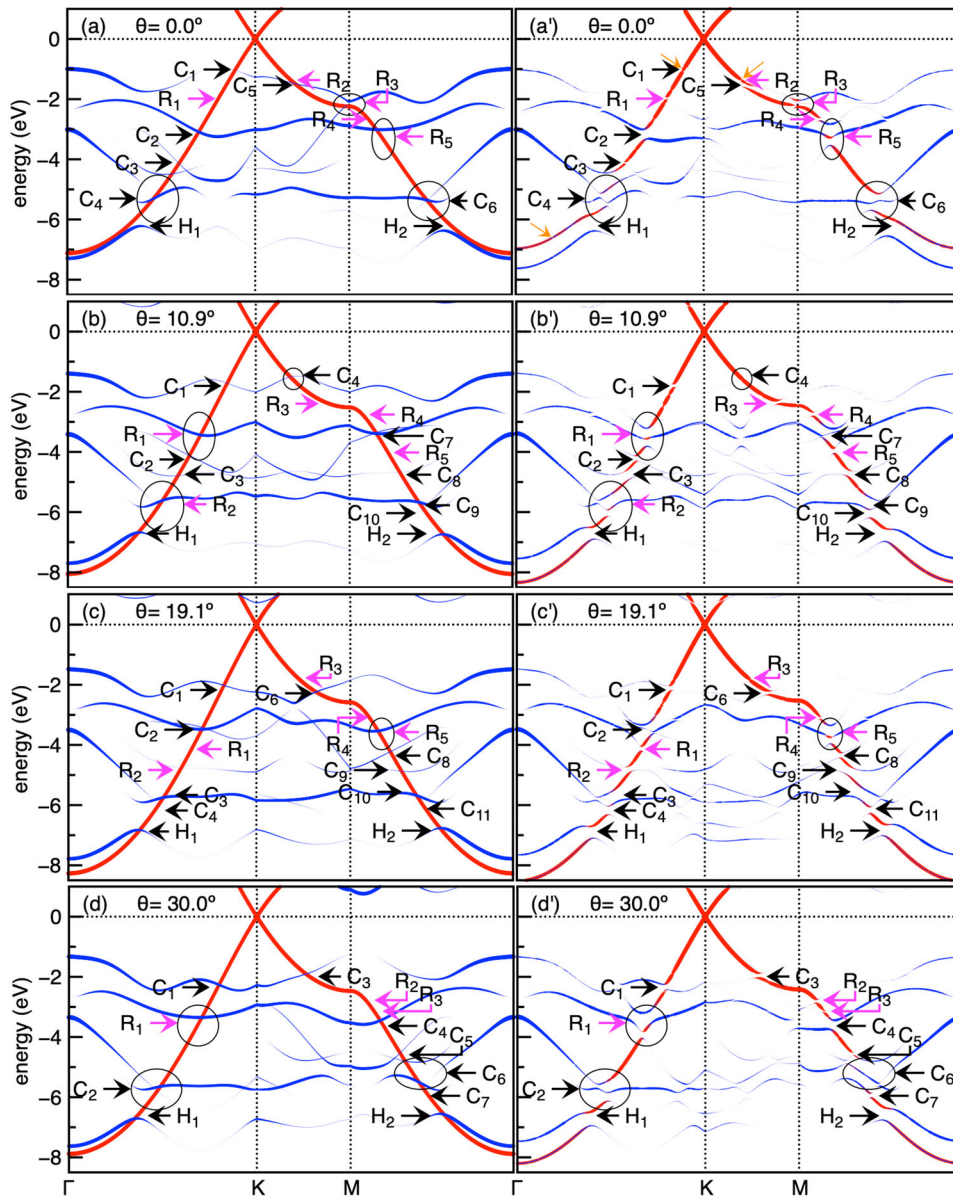
Fig. 6   Comparison between superposition of electronic bands of isolated G and WS$_2$ layers and effective electronic bands of G-WS$_2$ heterostructures. Left panels, **a**–**d**, show C($2p_z$) (red dots) and S($3p_z$) (blue dots) bands of isolated G and WS$_2$ layers projected on the G irreducible BZ for the different angles. Right panels, **a'**–**d'**, show the C($2p_z$) and S($3p_z$) EEBs for the corresponding four interacting G-WS$_2$ cases. The C_n, H_n, and R_n labels indicate mini-gaps associated with avoided crossings, hybridization, and superpotential replicas, respectively. The bands of isolated WS$_2$ are aligned such that the highest valence bands coincide on left-handed and right-handed side panels.

corresponding split band that is pushed down has more C($2p_z$) character than the one pushed up with more S($3p_z$) orbitals, and the energy gap are $\Delta E = 0.674$, 0.800, and 0.838 eV, respectively. By inspecting the spectral weights, W_k, it is found that the predominance of C($2p_z$) orbitals decrease as the compression strain increases.

All mini-gaps labeled as C_n arise from avoided crossing between C($2p_z$) and S($3p_z$)+W($5d_{z^2}$) bands, according to left-hand side panels in Fig. 6 for the isolated G and WS$_2$ layers. Some C_n mini-gaps exhibit a well-defined opening, particularly those bands that show a large spectral weight, W_k. For instance, mini-gaps labeled as C_2 in $\theta = 0.0$, 19.1°, and 30.0°, C_6 in $\theta = 0.0°$, C_9 in $\theta = 10.9°$, or C_{10} in $\theta = 19.1°$, all of them have predominance of S($3p_z$) orbitals. In contrast, bands with a small W_k, like the ones of S($3p_z$)+W($5d_{z^2}$) and energies close to E_F, open tiny gaps in the C($2p_z$) band in the four cases. These gaps are labeled as C_1. In particular, Fig. 6a, b

show that this band, where W($5d_{z^2}$) dominates, has a very small W_k, being quite imperceptible for the eye. However, our results reveal that W_k increases at this region for the cases with $\theta = 19.1$ and 30.0°, as seen in Fig. 6c, d, where S($3p_z$) orbitals dominate instead of W($5d_{z^2}$). In agreement, the right-hand side panels in Fig. 6 show more well-defined C_1 gaps as W_k increases. Notice that the band dispersion of S($3p_z$)+W($5d_{z^2}$) changes as a function of the twist-angle, shifting the energy where C_1 occurs as a function of θ, such that the position of C_1 mini-gap decreases in energy from ~ -1.0 to ~ -2.3 eV as the twist-angle increases from $\theta = 0.0$–30.0° despite the strain effect on G, as we show in the Supplementary Information. In conclusion, the larger weights of S($3p_z$)+W($5d_{z^2}$), the C_1 mini-gaps are lower energies, indeed, both effects of the interlayer rotation.

Although some avoided crossings nature is directly identified by doing a similar analysis of the electronic bands coming from the
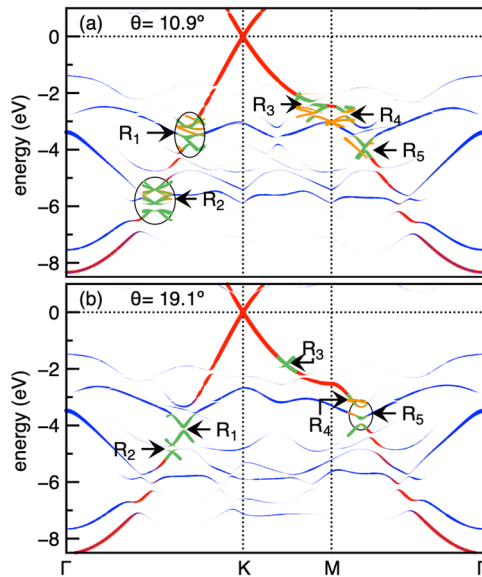
Fig. 7 Effective electronic bands and orbital analysis around R_n mini-gaps for the G-WS$_2$ at θ as the twist-angle. $\theta = $ **a** 10.9° and **b** 19.1°. C(2p$_z$) and S(3p$_z$) EEB are shown by red and blue dots. Green and orange dots display C(2p$_z$) and S(3p$_z$) contributions of bands replicas.

projected unit cells, as we did above, there are some mini-gaps whose origin is not discovered in this way. Let us analyze these mini-gaps, which are pointed with pink arrows in Fig. 6 and labeled as R_n, since they are associated with band replicas originated by the moiré superpotential. To gain a deeper insight into their origin, we analyze in Fig. 7 the bands replicas of C(2p$_z$) (green dots) and S(3p$_z$) (orange dots) at each R_n for the cases with $\theta = 10.9$ and 19.1°. Notice that these electronic states, in green and orange dots, do not belong to the projected unit cell but to the replicas. Let us analyze the $\theta = 10.9°$ case in detail. From Fig. 6b, b′, the R_3, R_4, and R_5 mini-gaps on EEB$_G$ (red dots) clearly lack of avoided crossing with EEB$_{WS_2}$ (blue dots). In Fig. 7a, R_3 emerges from a crossing with a WS$_2$ band replica with a small S(3p$_z$) character; R_4 does from a WS$_2$ band replica with a well-defined S(3p$_z$) character; and the R_5 comes from the crossing with a C(2p$_z$) band replica. In contrast, large band deviations observed in R_1 and R_2 mini-gaps suggest another kind of band interaction together with avoided crossing. For both mini-gaps, the presence of C(2p$_z$) and S(3p$_z$) replicas is observed. We find similar results for the $\theta = 19.1°$ case. Here, R_1 and R_3 emerge from C(2p$_z$) replicas; R_4 does from a crossing with a S(3p$_z$) replica; while R_2 and R_5 show a joint effect composed by a direct avoided crossing and that with C(2p$_z$) replicas.

From the above analysis, we infer that all R_n mini-gaps for $\theta = 0.0$ and 30.0°, shown in Fig. 6(a′) and (d′), respectively, emerge from a crossing between C(2p$_z$) and its replica or S(3p$_z$) replicas. Following the band behavior, we find that R_5 in $\theta = 0.0$ and R_1 for 30.0°, emerge from avoided crossing with S(3p$_z$) and C(2p$_z$) replicas, as it was noticed in R_1 for $\theta = 10.9°$ and R_5 for $\theta = 19.1°$. Although the strain condition imposed in G to obey commensurability, influences on its band dispersion, some $k-$ paths in the $\theta = 0.0°$ case are equivalent for $\theta = 30.0°$, such that most of mini-gaps also are. For instance, R_2, C_4, C_5, and C_6 along the Γ−M path for the $\theta = 30.0°$ case (see Fig. 6d′) are equivalent to R_1, C_2, C_3, and C_4 shown in the $\frac{4}{5}\Gamma$−K path of $\theta = 0.0°$, as seen in Fig. 6a′. Similarly, R_1 and C_2 along the $\frac{5}{6}\Gamma$−K path of $\theta = 30.0°$ coincide with R_5 and C_6 on M−Γ path when $\theta = 0.0°$. Such equivalence on these paths is confirmed by comparing the bands of the isolated WS$_2$ layer, shown in Fig. 6a, d.

Finally, we show how these mini-gaps relate the cone replicas to the mini Brillouin zones. Figure 5a shows the G-WS$_2$ reciprocal space for $\theta = 0.0°$. Despite that the four G-WS$_2$ systems exhibit two crossings with mini Brillouin zone borders over the Γ−K path of the G Brillouin zone and only one over K−M and M−Γ paths, respectively, the closeness and position of cone replicas over the Γ−K−M−Γ path change respect to the twist angle, θ, suggesting a control of the band gaps. In principle, each crossing border by a mini Brillouin zone, or the closeness to a cone replica, might induce a R_n mini-gap. For instance, R_1 and R_2 when $\theta = 0.0°$ coincide with crossings of mini Brillouin zone borders.

In conclusion, the relative twisted angle in bilayer heterostructure plays a relevant role in the appearance of band gaps and in controlling their energy values and sizes. These minigaps mainly originate from the repulsion between electronic states belonging to both layers, while Bragg diffractions induce only the slightest band deviations that are mostly imperceivable. However, avoided crossings between out-of-plane orbitals belonging to different layers open well-defined band gaps. Using an unfolding methodology to clear the supercell crowed bands and assign a spectral weight, we found that the gap size and band perturbations depend on the interactions revealed with the amount of the weight. It is worth mentioning that a specific control on the mini-gaps energy associated with the twisted angle can be mainly achieved along Γ−K or M−Γ paths. Besides avoided crossings, the superperiodic potential associated with the moiré pattern opens well-defined gaps on graphene or WS$_2$ band replicas. Other van der Waals heterostructures are expected to behave similarly, like WSe$_2$ systems, where minigaps might be localized at similar positions in the BZ but show a different gap size and energy position. However, detailed work must be done. Finally, we remark that the disclosure of mini-gaps and band distortions nature is only possible through an unfolding method to project the supercell wave functions onto each unit cell of its constituents.

METHODS

Initial structures

We started by optimizing the structural parameters of the pristine G and WS$_2$ hexagonal unit cells, giving $a_G = 2.44$ Å, and $a_{WS_2} = 3.16$ Å, for corresponding lattice constants. The average distances between C–C, W–S, and S$_{up}$–S$_{down}$ atoms are 1.41 Å, 2.41 Å, and 3.16 Å, respectively, also the average interlayer distance is 3.29 Å, which are all in agreement with experimental and theoretical reports[48,49]. With optimized lattice parameters, we constructed vertically stacked G-WS$_2$ 2D–vdW–h composed by one G sheet and one WS$_2$. Although both unit cells have hexagonal symmetry, lattice constants are different. So, G-WS$_2$ 2D–vdW–h must be set up by a supercell (SC). The use of SCs in electronic structure calculations has been a common practice due to the ongoing increase in computational resources. This has broadening the field of first-principles calculations towards systems with hundreds or thousands atoms, different composition, perturbations (like impurities), or combined systems such as vertically stacked 2D–vdW–h. In general, to generate a new structure starting from the original unit cell an affine transformation is involved, which consists of two parts: a linear part and a shift of the origin. The linear part implies a change of orientation or length or both of the basis vectors $\mathbf{a_1}$, $\mathbf{a_2}$, $\mathbf{a_3}$, which transform by a matrix $\mathbf{P}$ to a new basis vectors set $\mathbf{a'_1}$, $\mathbf{a'_2}$, $\mathbf{a'_3}$, i.e.:

$$\left(\mathbf{a'_1}, \mathbf{a'_2}, \mathbf{a'_3}\right) = \left(\mathbf{a_1}, \mathbf{a_2}, \mathbf{a_3}\right)\mathbf{P} = \left(\mathbf{a_1}, \mathbf{a_2}, \mathbf{a_3}\right)\begin{bmatrix} P_{11} & P_{12} & P_{13} \\ P_{21} & P_{22} & P_{23} \\ P_{31} & P_{32} & P_{33} \end{bmatrix} \quad (1)$$

In two dimensions, the new basis vectors set $\mathbf{a'_1}$, $\mathbf{a'_2}$, $\mathbf{a'_3}$ can be considered as a three dimensional transformation with invariant $\mathbf{a_3}$ axis[50]. Thus, $P_{33} = 1$ and $P_{13} = P_{23} = P_{31} = P_{32} = 0$. Hence, given

two integer indices (m, n), each layer is constructed by a matrix transformation **P** acting on its corresponding basis vector, such that **P** is now:

$$\mathbf{P} = \begin{bmatrix} m & n & 0 \\ -n & m+n & 0 \\ 0 & 0 & 1 \end{bmatrix} \quad (2)$$

For each G-WS$_2$ 2D–vdW–h studied here, it is required a couple of integer indices (m,n) and (p,q) for G and WS$_2$ layer, respectively, such that $m \geq n$ and $p \geq q$. Because of a_G/a_{WS_2} is not an integer number, we have imposed the condition that G layers have to be stretched or compressed to assure commensurability, while WS$_2$ remains its optimized lattice parameter. Hence, (m,n) and (p,q) must be chosen in such way that each layer obey commensurability. The stretching/compressing condition used in G layers induces a slight strain, Δ, which is obtained through[26]:

$$\Delta = \frac{a_G\sqrt{m^2+n^2+mn} - a_{WS_2}\sqrt{p^2+q^2+pq}}{a_{WS_2}\sqrt{p^2+q^2+pq}}. \quad (3)$$

The rotation angle (θ) between layers and the total number of atoms (N_t) in the G-WS$_2$ 2D–vdW–h are also defined by the (m,n) and (p,q) indices[26]:

$$\theta = \frac{mp + nq + (mq+np/2)}{\sqrt{m^2+n^2+mn} \times \sqrt{p^2+q^2+pq}}, \quad (4)$$

$$N_t = 3(m^2+n^2+mn) + 2(p^2+q^2+pq). \quad (5)$$

Commonly, supercells are expressed as ($u_1 \times u_2$), a notation obtained in terms of the magnitude of the projected lattice vectors of each SC into the lattice vectors of the pristine unit cell:

$$u_1 = \frac{|\mathbf{a}_{1,SC} \cdot \mathbf{a}_{1,X}|}{a_X}, \quad \text{and} \quad u_2 = \frac{|\mathbf{a}_{2,SC} \cdot \mathbf{a}_{2,X}|}{a_X}, \quad (6)$$

where subindex X denotes G or WS$_2$ layer. In this work, we set up four G-WS$_2$ 2D–vdW–h with different twisted-angle, $\theta = 0.0°$, 10.9°, 19.1°, and 30.0°. We use θ as the label of each heterostructure. Table 2 resumes the ($u_1 \times u_2$) notation for G and WS$_2$ layers, (m,n)

and (p,q) indices, N_t, θ, and Δ. We remark that induced strain in G layer is smaller than 4%.

Computational details

Total energy DFT calculations were performed using the computational code SIESTA[36]. The exchange-correlation energy was described by the local density approximation (LDA) functional[51]. The electron-ion interaction was treated with norm-conserving pseudopotentials[52] in their scalar relativistic and non-local form[53]. For the expansion of the electronic states, a linear combination of pseudoatomic orbitals (LCAO) was employed, with an optimized double-ζ polarized (DZP) basis set plus diffusive orbitals[54]. A mesh-cutoff energy of 300 Ry is applied to sample the electronic density in the real space. The electronic relaxation was converged to 10^{-5}. The Monkhorst–Pack scheme[55] was used for the Brillouin zone sampling with an optimal $21 \times 21 \times 1$ k-grid. A Fermi-Dirac smearing of 1 K is adopted to get convergence. The structural optimization was carried out with the conjugate gradient algorithm with a maximum value in the interatomic forces of 0.01 meV/Å, together with a value of 0.5 GPa in the stress components. Energy cutoff and k-grid convergence tests were performed on the four systems leading to the values as

Table 2. Structural parameters of the four G-WS$_2$ 2D–vdW–h studied here.

G-WS$_2$	$\theta = 0.0°$	$\theta = 10.9°$	$\theta = 19.1°$	$\theta = 30.0°$
$(u_1 \times u_2)_G$	(5×5)	$(2\sqrt{3} \times 2\sqrt{3})$	$(\sqrt{7} \times \sqrt{7})$	$(3\sqrt{3} \times 3\sqrt{3})$
$(u_1 \times u_2)_{WS_2}$	(4×4)	$(\sqrt{7} \times \sqrt{7})$	(2×2)	(4×4)
$(m,n);(p,q)$	$(5,0);(4,0)$	$(2,2);(2,1)$	$(2,1);(2,0)$	$(3,3);(4,0)$
N_t	98	45	26	102
$\Delta(\%)$	$+3.61$	-1.09	-2.10	-0.30
$K(k_x, k_y)^a$	$(5/3, 5/3)$	$(0, 2)$	$(1/3, 4/3)$	$(0, 3)$
$M(k_x, k_y)^b$	$(5/2, 0)$	$(-1, 2)$	$(-1/2, 3/2)$	$(-3/2, 3)$

^{a,b}Fractional coordinates (k_x, k_y) of equivalent K and M high-symmetry points of G in the reciprocal space of SC.
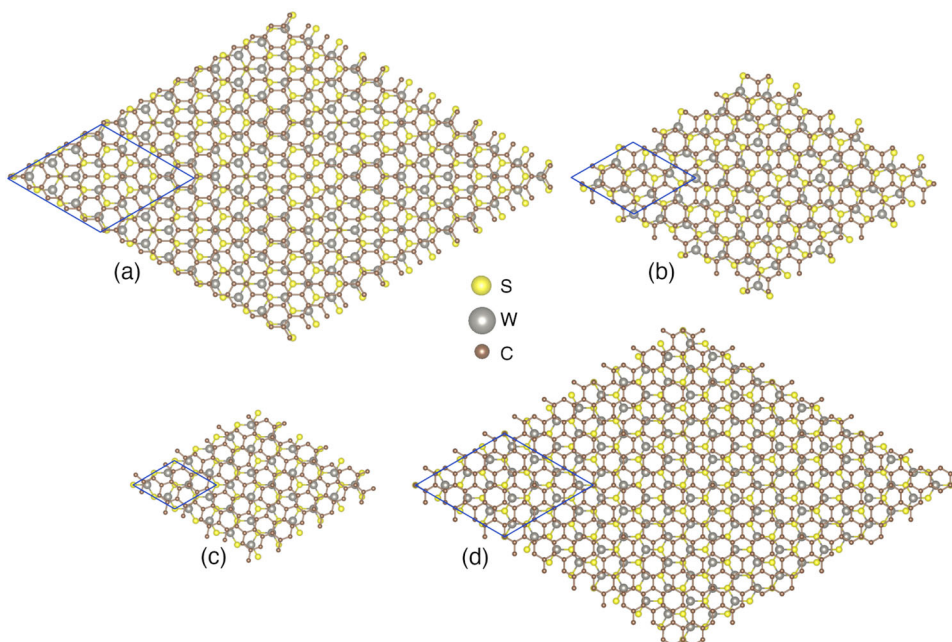

Fig. 8 Top view of ball-stick models of the four optimized 3×3 G-WS$_2$ supercell at θ as the twist-angle. $\theta =$ **a** 0.0°, **b** 10.9°, **c** 19.1°, and **d** 30.0°. Each supercell is marked by blue line.

mentioned earlier as the optimal ones. To avoid spurious interactions, a vacuum space of 55 Å between G and the bottom S layer in the next supercell is applied as well as a slab dipole correction associated with the vertical asymmetry of the heterostructure[56]. The zigzag directions of each system are taken as reference for the angle between G and WS_2[26]. Since both G and WS_2 systems have a hexagonal structure, the maximum limit of the rotation angle is 30°. Figure 8a–d shows the four G-WS_2 2D–vdW–h studied here. Visualization of atomic models are performed using the VESTA program[57].

DATA AVAILABILITY

The data that support the results of this study are included in the main text and/or the Supplementary Information. Additional data related to this paper may be available from the corresponding author C.N. (cecilia@fisica.unam.mx) upon reasonable request.

CODE AVAILABILITY

The code is available from the corresponding author upon a reasonable request.

REFERENCES

1. Geim, A. K. & Grigorieva, I. V. Van der waals heterostructures. *Nature* **499**, 419–425 (2013).
2. Bhimanapati, G. R. et al. Recent advances in two-dimensional materials beyond graphene. *ACS Nano* **9**, 11509–11539 (2015).
3. Zhang, W. et al. Ultrahigh–gain photodetectors based on atomically thin graphene–mos_2 heterostructures. *Sci. Rep.* **4**, 3826 (2014).
4. Georgiou, T. et al. Vertical field-effect transistor based on graphene–ws_2 heterostructures for flexible and transparent electronics. *Nat. Nanotechnol.* **8**, 100–103 (2013).
5. Lemme, M. C., Echtermeyer, T. J., Baus, M. & Kurz, H. A graphene field-effect device. *IEEE Electron Dev. Lett.* **28**, 282–284 (2007).
6. Daz, A. et al. Monitoring dopants by raman scattering in an electrochemically top-gated graphene transistor. *Nat. Nanotechnol.* **3**, 210–215 (2008).
7. Neto, A. H. C. Charge density wave, superconductivity, and anomalous metallic behavior in 2d transition metal dichalcogenides. *Phys. Rev. Lett.* **86**, 4382 (2001).
8. Akinwande, D., Petrone, N. & Hone, J. Two-dimensional flexible nanoelectronics. *Nat. Commun.* **5**, 5678 (2014).
9. Wu, W. et al. High mobility and high on/off ratio field-effect transistors based on chemical vapor deposited single-crystal mos_2 grains. *Appl. Phys. Lett.* **102**, 142106 (2013).
10. Ovchinnikov, D., Allain, A., Huang, Y.-S., Dumcenco, D. & Kis, A. Electrical transport properties of single-layer ws_2. *ACS Nano* **8**, 8174–8181 (2014).
11. Yu, W. J. et al. Vertically stacked multi-heterostructures of layered materials for logic transistors and complementary inverters. *Nat. Mater.* **12**, 246–252 (2013).
12. Liang, X., Fu, Z. & Chou, S. Y. Graphene transistors fabricated via transfer-printing in device active-areas on large wafer. *Nano Lett.* **7**, 3840–3844 (2007).
13. Kim, C.-J. et al. Chiral atomically thin films. *Nat. Nanotechnol.* **11**, 520–524 (2016).
14. Wang, Z. et al. Strong interface-induced spin-orbit interaction in graphene on ws_2. *Nat. Commun.* **6**, 8339 (2015).
15. Roy, K. et al. Graphene–mos_2 hybrid structures for multifunctional photo-responsive memory devices. *Nat. Nanotechnol.* **8**, 826–830 (2013).
16. Jin, W. et al. Direct measurement of the thickness-dependent electronic band structure of mos_2 using angle-resolved photoemission spectroscopy. *Phys. Rev. Lett.* **111**, 106801 (2013).
17. Li, G. et al. Observation of van hove singularities in twisted graphene layers. *Nat. Phys.* **6**, 109–113 (2010).
18. Gong, Y. et al. Vertical and in-plane heterostructures from ws_2/mos_2 monolayers. *Nat. Mater.* **13**, 1135–1142 (2014).
19. Mak, K. F., Lee, C., Hone, J., Shan, J. & Heinz, T. F. Atomically thin mos_2: a new direct-gap semiconductor. *Phys. Rev. Lett.* **105**, 136805 (2010).
20. dos Santos, J. M. B. L., Peres, N. M. R. & Neto, A. H. C. Graphene bilayer with a twist: electronic structure. *Phys. Rev. Lett.* **99**, 256802 (2007).
21. Wang, Y. et al. Stacking-dependent optical conductivity of bilayer graphene. *ACS Nano* **4**, 4074–4080 (2010).
22. Landgraf, W., Shallcross, S., Türschmann, K., Weckbecker, D. & Pankratov, O. Stacking-dependent optical conductivity of bilayer graphene. *Phys. Rev. B* **87**, 075433 (2013).
23. Sánchez-Ochoa, F., Botello-Méndez, A. R. & Noguez, C. Angle-dependent electron confinement in graphene moiré superlattices. *Phys. Rev. B* **104**, 075430 (2021).
24. Wang, Z., Chen, Q. & Wang, J. Electronic structure of twisted bilayers of graphene/mos_2 and mos_2/mos_2. *J. Phys. Chem. C* **119**, 4752–4758 (2015).
25. Felice, D. D., Abad, E., Gonzúlez, C., Smogunov, A. & Dappe, Y. J. Angle dependence of the local electronic properties of the graphene/mos_2 interface determined by ab initio calculations. *J. Phys. D Appl. Phys.* **50**, 17 (2017).
26. Li, L. & Zhao, M. Structures, energetics, and electronic properties of multifarious stacking patterns for high-buckled and low-buckled silicene on the mos_2 substrate. *J. Phys. Chem. C* **118**, 19129–19138 (2014).
27. Sa, B., Sun, Z. & Wu, B. The development of two dimensional group iv chalcogenides, blocks for van der waals heterostructures. *Nanoscale* **8**, 1169 (2016).
28. Wang, Y. & Ding, Y. The electronic structures of group–v–group–iv hetero-bilayer structures: a first-principles study. *Phys. Chem. Chem. Phys.* **17**, 27769–27776 (2015).
29. Wang, Y. et al. All-metallic vertical transistors based on stacked dirac materials. *Adv. Funct. Mater.* **25**, 68–77 (2015).
30. Pierucci, D. et al. Band alignment and minigaps in monolayer mos_2-graphene van der waals heterostructures. *Nano Lett.* **16**, 4054–4061 (2016).
31. Diaz, H. C. et al. Direct observation of interlayer hybridization and dirac relativistic carriers in graphene/mos_2 van der waals heterostructures. *Nano Lett.* **15**, 1135–1140 (2015).
32. Medeiros, P. V. C. et al. Effects of extrinsic and intrinsic perturbations on the electronic structure of graphene: retaining an effective primitive cell band structure by band unfolding. *Phys. Rev. B* **89**, 041407 (2014).
33. Medeiros, P. V. C. et al. Unfolding spinor wave functions and expectation values of general operators: introducing the unfolding-density operator. *Phys. Rev. B* **91**, 041116 (2015).
34. Le, N. B., Huan, T. D. & Woods, L. M. Interlayer interactions in van der waals heterostructures: electron and phonon properties. *ACS Appl. Mater. Interfaces* **8**, 6286–6292 (2016).
35. Si, C., Sun, Z. & Liu, F. Strain engineering of graphene: a review. *Nanoscale* **8**, 3207–3217 (2016).
36. Soler, J. M. et al. The siesta method for ab initio order-n materials simulation. *J. Phys.: Condens. Matter* **14**, 2745 (2002).
37. Ku, W., Berlijn, T. & Lee, C.-C. Unfolding first-principles band structures. *Phys. Rev. Lett.* **104**, 216401 (2010).
38. Popescu, V. & Zunger, A. Effective band structure of random alloys. *Phys. Rev. Lett.* **104**, 236403 (2010).
39. Popescu, V. & Zunger, A. Extracting e versus $\vec{k}$ effective band structure from supercell calculations on alloys and impurities. *Phys. Rev. B* **85**, 085201 (2012).
40. Lee, C.-C., Yamada-Takamura, Y. & Ozaki, T. Unfolding method for first-principles lcao electronic structure calculations. *J. Phys. Condens. Matter* **25**, 345501 (2013).
41. Boykin, T. B. & Klimeck, G. Practical application of zone-folding concepts in tight-binding calculations. *Phys. Rev. B* **71**, 115215 (2005).
42. Boykin, T. B., Kharche, N., Klimeck, G. & Korkusinski, M. Approximate band-structures of semiconductor alloys from tight-binding supercell calculations. *J. Phys. Condens. Matter* **19**, 036203 (2007).
43. Nishi, H., Matsushita, Y.-i. & Oshiyama, A. Band-unfolding approach to moiré-induced band-gap opening and fermi level velocity reduction in twisted bilayer graphene. *Phys. Rev. B* **95**, 085420 (2017).
44. Sánchez-Ochoa, F., Hidalgo, F., Pruneda, M. & Noguez, C. Unfolding method for periodic twisted systems with commensurate moiré patterns. *J. Phys. Condens. Matter* **32**, 025501 (2019).
45. Marinopoulos, A. G., Reining, L., Rubio, A. & Olevano, V. Ab initio study of the optical absorption and wave-vector-dependent dielectric response of graphite. *Phys. Rev. B* **69**, 245419 (2004).
46. Pletikosić, I. et al. Dirac cones and minigaps for graphene on ir(111). *Phys. Rev. Lett.* **102**, 056808 (2009).
47. Polley, C. M. et al. Origin of the π-band replicas in the electronic structure of graphene grown on 4h-sic(0001). *Phys. Rev. B* **99**, 115404 (2019).
48. Li, S.-S. & Zhang, C.-W. First-principles study of graphene adsorbed on $ws2$ monolayer. *J. Appl. Phys.* **114**, 183709 (2013).
49. Kaloni, T. P., Kou, L., Frauenheim, T. & Schwingenschlögl, U. Quantum spin hall states in graphene interacting with $ws2$ or $wse2$. *Appl. Phys. Lett.* **105**, 233112 (2014).
50. Arnold, H. *International Tables for Crystallography*. Vol. A, Chapter 5.1 (Springer, 2006).
51. Perdew, J. P. & Zunger, A. Self-interaction correction to density-functional approximations for many-electron systems. *Phys. Rev. B* **23**, 5048 (1981).
52. Hamann, D. R., Schlüter, M. & Chiang, C. Norm-conserving pseudopotentials. *Phys. Rev. Lett.* **43**, 1494–1497 (1979).
53. Kleinman, L. & Bylander, D. M. Efficacious form for model pseudopotentials. *Phys. Rev. Lett.* **48**, 1425–1428 (1982).

54. García-Gil, S., García, A., Lorente, N. & Ordejón, P. Optimal strictly localized basis sets for noble metal surfaces. *Phys. Rev. B* **79**, 075441 (2009).

55. Monkhorst, H. J. & Pack, J. D. Special points for brillouin-zone integrations. *Phys. Rev. B* **13**, 5188 (1976).

56. Bengtsson, L. Dipole correction for surface supercell calculations. *Phys. Rev. B* **59**, 12301–12304 (1999).

57. Momma, K. & Izumi, F. Vesta3 for three-dimensional visualization of crystal, volumetric and morphology data. *J. Appl. Crystallogr.* **44**, 1272–1276 (2011).

AUTHOR CONTRIBUTIONS

C.N. conceived the work. F.H. performed the DFT calculations. F.S.O. applied the unfolding electronic bands method. All authors discussed and analyzed the results and participated in the writing of the manuscript.

COMPETING INTERESTS

The authors declare no competing interests.

ADDITIONAL INFORMATION

Supplementary information The online version contains supplementary material available at https://doi.org/10.1038/s41699-023-00398-w.

Correspondence and requests for materials should be addressed to Cecilia Noguez.

Reprints and permission information is available at http://www.nature.com/reprints

Publisher's note Springer Nature remains neutral with regard to jurisdictional claims in published maps and institutional affiliations.